




**Electrical conductivity of a warm neutron star crust in magnetic fields: Neutron-drip regime**Arus Harutyunyan <sup>1,2,\*</sup> Armen Sedrakian <sup>3,4,†</sup> Narine T. Gevorgyan,<sup>1,5,‡</sup> and Mekhak V. Hayrapetyan <sup>2,§</sup><sup>1</sup>*Byurakan Astrophysical Observatory, Byurakan 0213, Armenia*<sup>2</sup>*Department of Physics, Yerevan State University, Yerevan 0025, Armenia*<sup>3</sup>*Frankfurt Institute for Advanced Studies, D-60438 Frankfurt am Main, Germany*<sup>4</sup>*Institute of Theoretical Physics, University of Wrocław, 50-204 Wrocław, Poland*<sup>5</sup>*A.I. Alikhanyan National Science Laboratory (Yerevan Physics Institute), Yerevan 0025, Armenia*

(Received 18 September 2023; revised 29 January 2024; accepted 29 April 2024; published 22 May 2024)

We compute the anisotropic electrical conductivity tensor of the inner crust of a compact star at nonzero temperature by extending a previous work on the conductivity of the outer crust. The physical scenarios, where such crust is formed, involve protoneutron stars born in supernova explosions, binary neutron star mergers, and accreting neutron stars. The temperature-density range studied covers the transition from a semidegenerate to a highly degenerate electron gas and assumes that the nuclei form a liquid, i.e., the temperature is above the melting temperature of the lattice of nuclei. The electronic transition probabilities include (i) the screening of electron-ion interaction in the hard-thermal-loop approximation for the QED plasma, (ii) the correlations of the ionic component in a one-component plasma, and (iii) finite nuclear size effects. The conductivity tensor is obtained from the Boltzmann kinetic equation in relaxation time approximation accounting for the anisotropy introduced by a magnetic field. The sensitivity of the results towards the matter composition of the inner crust is explored by using several compositions of the inner crust, which were obtained using different nuclear interactions and methods of solving the many-body problem. The standard deviations of relaxation time and components of the conductivity tensor from the average are below  $\leq 25\%$  except close to crust-core transition, where nonspherical nuclear structures are expected. Our results can be used in dissipative magnetohydrodynamics simulations of warm compact stars.

DOI: [10.1103/PhysRevC.109.055804](https://doi.org/10.1103/PhysRevC.109.055804)**I. INTRODUCTION**

The knowledge of transport properties of hot baryonic matter is important for large-scale magnetohydrodynamics description of astrophysical phenomena associated with compact stars. One such setting offer binary neutron star (BNS) mergers, such as the GW170817 event [1]: matter is expected to be heated both in the postmerger and premerger phases. In the postmerger phase, the matter is heated to temperatures up to 100–150 MeV by deposition of kinetic and gravitational energy in the matter; in the premerger phase, the matter may be heated via the dissipation of the energy of the tidally induced oscillations. Another longer time-scale setting is offered by the accreting neutron stars as their crusts are heated through the in-falling matter and the onset of nuclear reactions in various crustal layers. The warm matter regime is of interest also in the context of transient protoneutron stars born in supernova explosions. In this work we focus on stellar matter at subnuclear densities at moderate temperatures in the range  $T_m \leq T \leq T_{tr}$ , where  $T_m \simeq 1$  MeV is the melting temperature

of the crustal lattice corresponding to matter featuring heavy nuclei, dripped neutrons, and relativistic electron gas in liquid matter regime and  $T_{tr} \simeq 5$  MeV is the trapping temperature of neutrinos.

Transport in compact star plasma has been extensively studied in the cold and dense limit where it is dominated by the degenerate fermionic quantum liquids over a long period; for general reviews see Refs. [2,3]. More recently, the electrical conductivity of the warm outer crust was computed in Ref. [4] in the context of BNS mergers; it also provides a detailed review of the previous work on the conductivity of crustal matter in the cold regime, which we do not repeat here. The conductivity tensor of Ref. [4] was then used to assess its importance in the dynamics of BNS mergers [5], showing the conditions for the breakdown of the ideal magnetohydrodynamics limit and the importance of the Hall conductivity.

This paper extends a previous calculation of the conductivity of heated crustal matter in nonquantizing magnetic fields [4] to the inner crust phase where along with the crustal lattice, there is an unbound neutron component. Our focus is on the case with spherical nuclei for which several compositions [6–9] will be used. Our collection includes two models with zero-range Skyrme interaction [8,9], which use modern and accurate parametrizations of this force, see also Ref. [10]. The two models of Ref. [7] use modern parametrizations of the finite-range Gogny interaction. We also included the widely

\* arus@bao.sci.am

† sedrakian@fias.uni-frankfurt.de

‡ gevorgyan.narine@gmail.com

§ mhayrapetyan@ysu.am

used model of Ref. [6], which is based on a density-dependent effective Hamiltonian tuned on finite nuclei; see Sec. II for a further discussion of these models. The conductivity of pasta phases where the shapes and topologies of nuclei deviate strongly from the spherical within the layer between the stellar core and the phase with spherical nuclei was studied in Ref. [11]. The low-temperature regime of electrical and thermal conductivity, where the nuclei form a lattice and interactions are mediated by lattice phonons was studied in Ref. [12]. We will restrict our discussion to magnetic fields below  $B_c \simeq 10^{14}$  G. Above these values, the Landau quantization of electron trajectories must be taken into account, see Ref. [13].

The paper is organized as follows. In Sec. II we review the compositions of the neutron star's inner crust, which are used in our computations of the electrical conductivity tensor. Section III collects the relevant ingredients of the formalism and key results, which have been presented in detail in Ref. [4]. Our numerical results are discussed in Sec. IV. The final Sec. V contains a summary of our results. We use the natural (Gaussian) units with  $\hbar = c = k_B = k_e = 1$ ,  $e = \sqrt{4\pi}$ ,  $\alpha = 1/137$ , and the metric signature  $(1, -1, -1, -1)$ .

## II. EQUATION OF STATE, COMPOSITION AND PHYSICAL CONDITIONS IN INNER CRUST

Above the neutron drip density  $\rho_{\text{drip}} = 4.3 \times 10^{11}$  g cm<sup>-3</sup> a phase transition takes place in neutron star crusts: the low-density phase consisting of fully ionized nuclei, which are characterized by the nucleon number  $A$  and proton number  $Z$ , and relativistic electrons is replaced by a phase, which in addition to the components of the low-density phase has also unbound neutrons. Then, the total baryon density  $n_B$  is given by

$$n_B = An_i + n'_n, \quad (1)$$

where  $n_i$  is the number density of the ions (nuclei) and  $n'_n = (1 - V_N n_i)n_n$ , where  $n_n$  is the number density of unbound neutrons,  $V_N$  is the volume of the nucleus, and the term  $V_N n_i$  is the excluded volume correction [14]. The ion-electron subsystem, viewed as Coulomb plasma, is characterized by the parameters

$$\Gamma = \frac{T_C}{T}, \quad T_C = \frac{e^2 Z^2}{a_i}, \quad (2)$$

where  $e$  is the elementary charge,  $T$  is the temperature,  $a_i = (4\pi n_i/3)^{-1/3}$  is the radius of the spherical volume per ion, i.e., that of the Wigner-Seitz cell. For  $\Gamma \ll 1$  ( $T \gg T_C$ ) ions are weakly coupled and because of their large mass they form a classical Boltzmann gas. When  $\Gamma \geq 1$  ions are strongly coupled and form a solid phase with nuclei arranged in a regular lattice for  $\Gamma > \Gamma_m \simeq 160$ . In the opposite case  $\Gamma < \Gamma_m$  the liquid phase is energetically preferred. The temperature of melting of the crustal lattice is given by  $T_m = T_C/\Gamma_m$ . The lattice plasma temperature is defined as

$$T_p = \left( \frac{4\pi Z^2 e^2 n_i}{M} \right)^{1/2}, \quad (3)$$

where  $M$  is the ion mass. (Note that in units where  $\hbar = 1$ , the plasma frequency and plasma temperature coincide). The quantum regime for ion lattice (under which the quantization of oscillations of the lattice is required) occurs for  $T \leq T_p$ .

For numerical computations, we will adopt five different density-dependent compositions of stellar matter for the inner crust of a neutron star, which we label as NV [6], D1M and D1M\* [7], Bsk24 [8], and Sly9 [9]. These compositions were computed at  $T = 0$ . Reference [6] starts with the density-dependent Hartree-Fock theory and performs density matrix expansion to write down a Hamiltonian, which depends on the densities of protons and neutrons and their gradients. The model of the inner crust is then obtained by minimizing the energy per nucleon of spherically symmetric configurations of nucleons in a Wigner-Seitz unit cell with a uniform background gas of degenerate electrons. The pairing correlations and shell effects were neglected. Despite its limitations, the model of Ref. [6] has been used in astrophysical applications extensively, in particular, in the studies of transport in the solid regime at low temperatures [12]. The two models of Ref. [7] were obtained using finite-range Gogny interactions to obtain the nuclear mean field and pairing correlations self-consistently. The model of the inner crust was obtained using the semiclassical variational Wigner-Kirkwood method, which incorporated both shell and pairing corrections, which were, respectively, computed using the Strutinsky integral and the Bardeen-Cooper-Schrieffer (BCS) mean-field approximation. The model of Ref. [8], see also Ref. [10], uses zero-range Bsk24 Skyrme functional from the family of Brussels-Montreal nuclear density functionals and computes the properties of the inner crust using the temperature-dependent extended Thomas-Fermi method, supplemented with Strutinsky integral method to account for shell effects and BCS pairing through inclusion of BCS pairing energy in the density functional. Reference [9] uses zero-range Skyrme functional for unbound particles and beyond drip-line nuclei and realistic nuclear mass and level density tables for known nuclei in a model of a statistical distribution of Wigner-Seitz cells. It includes phenomenological pairing correction term that scales with mass number and the shell effects are accounted for automatically in the experimental data used.

We will assume below that the composition does not depend strongly on the temperature in the range of temperatures studied here so that the background composition of the inner crust in each case will be fixed at the one derived for  $T = 0$ . The physical conditions change significantly with the increasing temperature at about  $T_{\text{tr}} \simeq 5$  MeV where the neutrinos become trapped and  $\beta$ -equilibrium conditions are changed. As the temperature is further increased the appearance of lighter clusters—deuterons, tritons, helions, and alpha particles become possible for temperatures  $T \geq 10$  MeV [15–20]. Their contribution to conductivity is left for future study.

Figure 1 shows the proton number  $Z$  and the nucleon number  $A$  of the nuclei as functions of the net mass density for the chosen compositions of the stellar matter. Up to densities  $\log_{10} \rho$  [g cm<sup>-3</sup>]  $\leq 13$  all predict  $Z = 40$  semimagic proton values. Above these densities, Bsk24 and D1M\* predict the same  $Z = 40$  value, NV composition predicts the magic value

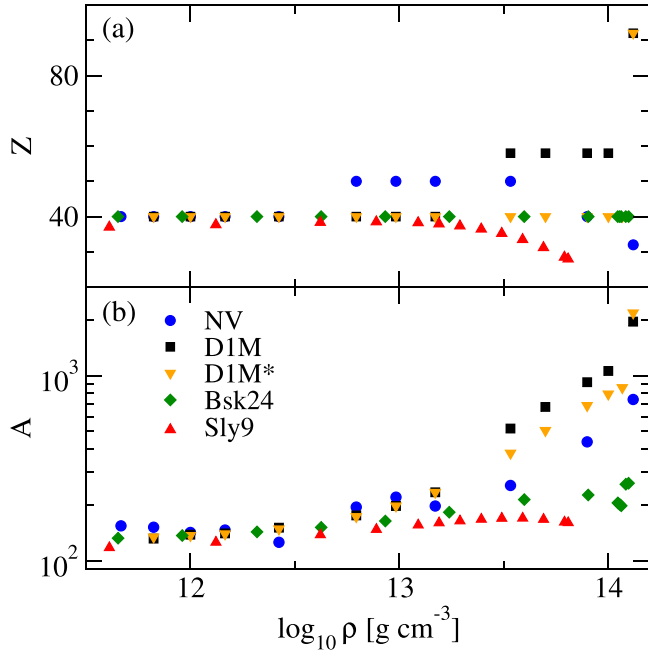


FIG. 1. The proton number  $Z$  (top panel) and the nucleon number  $A$  (bottom panel) of the nuclei as functions of the mass density for five different compositions of the stellar matter labeled as NV [6], D1M and D1M\* [7], Bsk24 [8], and Sly9 [9].

$Z = 50$  (except the last point) whereas D1M and Sly9 predict higher and lower  $Z$  values, respectively. Therefore, the matrix elements for the electron scattering off the individual nuclei are nearly the same for these compositions at low densities but deviate at higher densities. However, since the transport depends on the average number of nuclei per unit volume, such factors as the free neutron density and the mass number of a nucleus are important, see Eq. (1), which nontrivially modify the predictions based on the value of  $Z$ .

Figure 2 shows the fraction of free neutrons  $Y_n = n'_n/n_B$  defined as the ratio of the number of free neutrons to that of all nucleons in the Wigner-Seitz cell and the ion number density as functions of the mass density for all five compositions studied. Notable deviations are seen in free neutron fractions in the high-density range  $13 \leq \log_{10} \rho [\text{g cm}^{-3}] \leq 14$ , where the models D1M and D1M\* predict decreasing free neutron fractions because of the fast increase of the nuclear mass number  $A$  at these densities. In the models Bsk24 and Sly9  $Y_n$  remains almost constant ( $Y_n \simeq 0.8$ ) at  $\log_{10} \rho [\text{g cm}^{-3}] \geq 13$ , whereas the model NV shows somewhat intermediate behavior between these two model types at  $\log_{10} \rho [\text{g cm}^{-3}] \geq 13.5$  where the neutron fraction drops again.

Figure 3 shows the phase diagram of the matter in the inner crust of neutron stars in the temperature-density plane for five compositions. In the top part of the diagram where  $T > T_C$  the ionic component forms a weakly interacting Boltzmann gas, as the thermal energy exceeds the Coulomb interaction energy. In the bottom part of the diagram where  $T < T_m$  the ionic component solidifies, i.e., the scattering of electrons is (predominantly) on the phonons of the lattice. The plasma temperature  $T_p$  is lower than the melting temperature for the

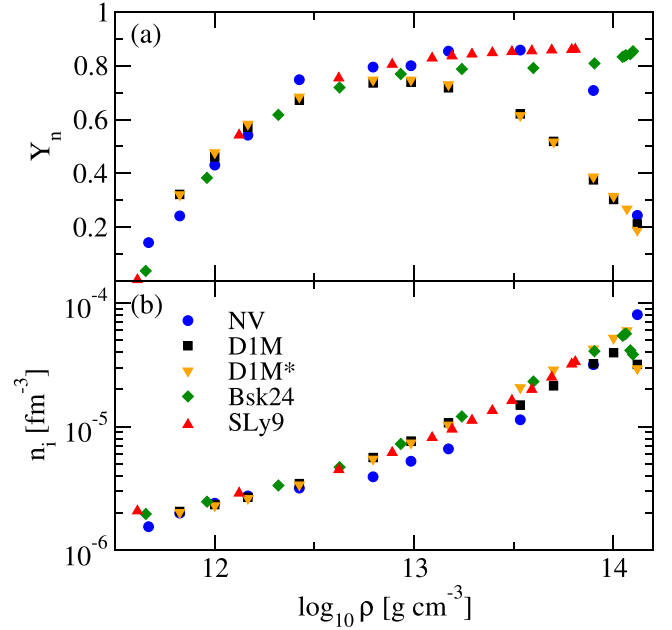


FIG. 2. (a) The fraction of free neutrons  $Y_n = n'_n/n_B$  and (b) the number density of ions as functions of the mass density for five compositions of stellar matter.

five models in Fig. 3 and is not shown. Our results apply in the regime where  $T > T_m$ . Note the weak density and model dependence of the curves  $T_m(\rho)$  and  $T_C(\rho)$  (except the region  $\log_{10} \rho [\text{g cm}^{-3}] \geq 13.5$ ).

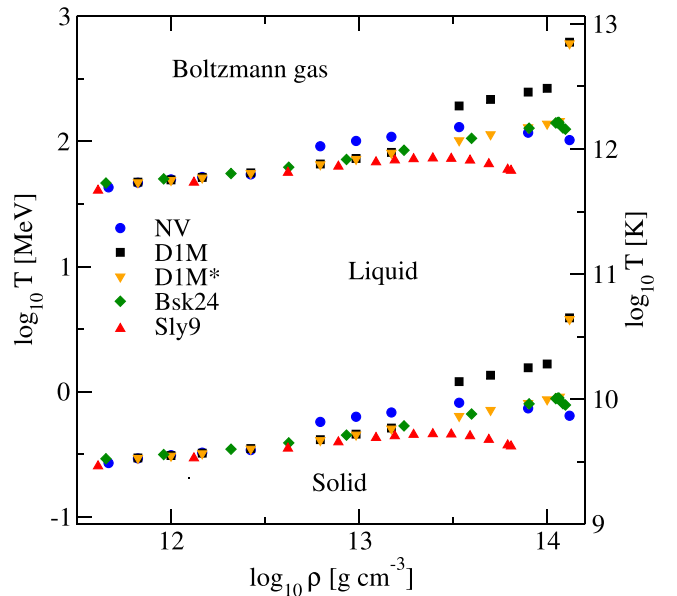


FIG. 3. The phase diagram of dense plasma in the inner crust of the neutron star in the temperature-density plane for five different compositions. The lower curves show the melting temperature  $T_m$  below which the ionic component solidifies. Upper curves show  $T_C$  above which the ionic component forms a Boltzmann gas. The present study covers the liquid portion of the phase diagram.

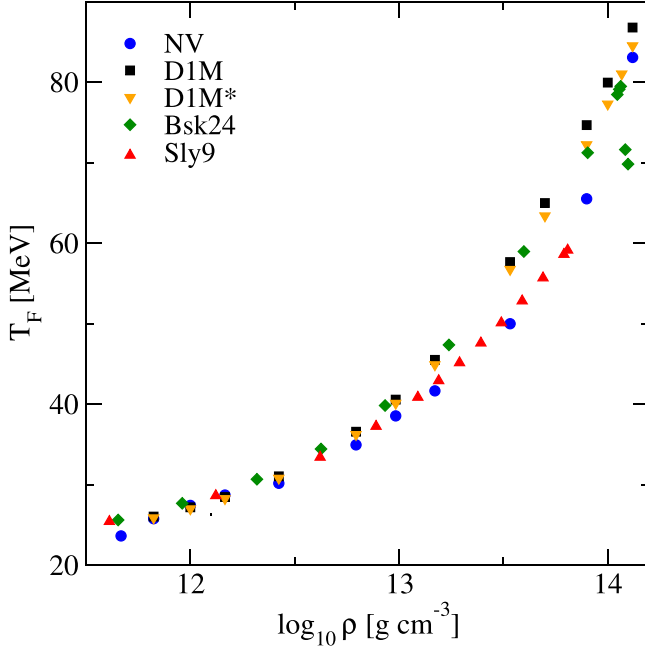


FIG. 4. The Fermi temperature  $T_F$  of the electronic component of the stellar matter in the inner crust of a neutron star for five different compositions shown in Fig. 1. The electron gas is becoming gradually nondegenerate above and degenerate below this temperature.

The transport in the liquid phase of a neutron star's inner crust is controlled by the electrons, which, to a good approximation, can be treated as a free Fermi gas except for the collisions with ions that lead to dissipation contributing to conductivity. (Electron-electron interaction can affect the conductivity indirectly by modifying the density of state of electrons, but the correction is a higher-order effect in the fine structure constant). The electron density is obtained from the charge conservation  $n_e = Zn_i$  and allows us to define their low-temperature characteristics, such as Fermi energy  $\varepsilon_F = (p_F^2 + m^2)^{1/2}$  and temperature  $\varepsilon_F - m \equiv T_F$ , where  $m$  is the electron mass and  $p_F = (3\pi^2 n_e)^{1/3}$  is the Fermi momentum. Note that at densities considered in this paper electrons are ultrarelativistic therefore we have, in practice,  $T_F = \varepsilon_F = p_F$ .

The Fermi temperature for five compositions is shown in Fig. 4. It is seen that electrons are degenerate up to a quite high temperature of several tens of MeV. This is in contrast to the outer crust region [4], where low densities required treatment of the transition from degenerate to the nondegenerate regime. Nevertheless, as our setup works across from nondegenerate to strongly degenerate limits, no additional limitations are imposed. Overall, we see that electrons are degenerate or semidegenerate for the temperatures relevant to BNS mergers and core-collapse supernovas at densities relevant to compact star inner crust. We recall that our discussion is limited to temperatures below several MeV, as the compositions adopted will be modified due to finite-temperature effects at larger temperatures. In addition, to modifications of thermodynamics, additional species such as alpha particles and other light clusters will appear in the matter [15–20] and will contribute to the conductivity. As a consequence, we will focus on the

degenerate electron regime while providing some extrapolation to higher temperatures, which are suggestive of the behavior of various quantities.

### III. CONDUCTIVITY IN MAGNETIC FIELD FROM BOLTZMANN EQUATION

In this section, we provide the key ingredients of the formalism presented extensively in Ref. [4], which is based on the (quasi)particle transport of electrons in strong magnetic fields. The kinetics of electrons is described by the Boltzmann equation for the electron distribution function

$$\frac{\partial f}{\partial t} + \mathbf{v} \frac{\partial f}{\partial \mathbf{r}} - e(\mathbf{E} + [\mathbf{v} \times \mathbf{B}]) \frac{\partial f}{\partial \mathbf{p}} = I[f], \quad (4)$$

where  $\mathbf{E}$  and  $\mathbf{B}$  are the electric and magnetic fields,  $\mathbf{v}$  is the electron velocity,  $e$  is the unit charge, and  $I[f]$  is the collision integral, which for electron-ion collisions has the form

$$I = -(2\pi)^4 \sum_{234} |\mathcal{M}_{12 \rightarrow 34}|^2 \delta^{(4)}(p + p_2 - p_3 - p_4) \times [f(1 - f_3)g_2 - f_3(1 - f)g_4], \quad (5)$$

where  $f = f(p)$  and  $f_3 = f(p_3)$  are the distribution functions of the incoming and outgoing electron,  $g_{2,4} = g(p_{2,4})$  are the distribution functions of the ion before and after a collision, and we introduced the shorthand notation:  $\sum_i = \int d\mathbf{p}_i / (2\pi)^3$ .

As discussed above, ions form a classical liquid in equilibrium with the Maxwell-Boltzmann distribution, i.e.,

$$g(p) = n_i \left( \frac{2\pi}{MT} \right)^{3/2} \exp \left( -\frac{p^2}{2MT} \right). \quad (6)$$

The range of validity of the kinetic equation (4) follows from the common considerations of the kinetic theory [21]. Specifically, it is assumed that the collisions are instantaneous, i.e., the distribution function is tracked only in between collisions. Similarly, we assumed that the range of scattering (effective size of screened Coulomb field  $d$ ) is much smaller than mean-free path  $\bar{l}$  between collisions. If the perturbations of the system are characterized by characteristic length  $L$  and frequency  $\Omega$  (for example  $L$  could be the scale set by gradients of electromagnetic potentials and  $\Omega$  the frequency of oscillations) the general validity condition can be written as

$$d \ll \bar{l} \ll L, \quad \bar{\tau} \ll \Omega^{-1},$$

where  $\bar{\tau}$  is the mean-free flight time associated with  $\bar{l}$ , which is of the order of the relaxation time of distribution function, see below. Next, consider small perturbations  $\delta f$  around the equilibrium Fermi-Dirac distribution function of electrons to linearize the Boltzmann equation:  $f = f^0 + \delta f$ ,  $\delta f \ll f_0$ , where the equilibrium distribution is given by

$$f^0(\varepsilon) = \frac{1}{e^{(\varepsilon - \mu)/T} + 1}, \quad (7)$$

with the spectrum of noninteracting electrons given by  $\varepsilon = \sqrt{p^2 + m^2}$ , and  $\mu$  is the electron chemical potential. Since we are interested in the electrical conductivity we keep only the last term on the left-hand side of Eq. (4). Substituting  $f = f^0 + \delta f$  in Eq. (4) and decomposing  $\delta f$  in terms of

independent tensor components containing the electric and magnetic fields we obtain [4]

$$\delta f = \frac{e\tau}{1 + (\omega_c\tau)^2} \frac{\partial f^0}{\partial \varepsilon} v_i [\delta_{ij} - \omega_c\tau \epsilon_{ijk} b_k + (\omega_c\tau)^2 b_i b_j] E_j, \quad (8)$$

where  $\mathbf{b} \equiv \mathbf{B}/B$ ,  $\omega_c = eB/\varepsilon$  is the cyclotron frequency for electrons, and the Latin indices label the components of Cartesian coordinates. Here we work in the relaxation-time approximation with the relaxation time defined by

$$\tau^{-1}(\varepsilon) = (2\pi)^{-5} \int d\mathbf{q} \int d\mathbf{p}_2 |\mathcal{M}_{12 \rightarrow 34}|^2 \frac{\mathbf{q} \cdot \mathbf{p}}{p^2} \times \delta(\varepsilon + \varepsilon_2 - \varepsilon_3 - \varepsilon_4) g_2 \frac{1 - f_3^0}{1 - f^0}, \quad (9)$$

The electrical conductivity is then obtained by computing the electrical current

$$\mathbf{j}_i = -2 \int \frac{d\mathbf{p}}{(2\pi)^3} e v_i \delta f = \sigma_{ij} E_j. \quad (10)$$

Substituting Eq. (8) in Eq. (10) and we find

$$\sigma_{ij} = \delta_{ij} \sigma_0 - \epsilon_{ijm} b_m \sigma_1 + b_i b_j \sigma_2, \quad (11)$$

where

$$\sigma_n = \frac{e^2}{3\pi^2 T} \int_m^\infty d\varepsilon \frac{p^3}{\varepsilon} \frac{\tau(\omega_c\tau)^n}{1 + (\omega_c\tau)^2} f^0(1 - f^0), \quad n = 0, 1, 2. \quad (12)$$

The matrix element includes several corrections to the bare Coulomb interaction between an electron and an ion. The screening of the interaction is taken into account via the hard-thermal-loop polarization tensor of QED, see Sec. IV D of Ref. [4]. The ion-ion correlations are taken by using fits to the structure factor  $S(q)$  of one-component plasma for various values of plasma parameter  $\Gamma$  obtained from Monte Carlo computations, see Fig. 4 of Ref. [4]. Finally, the finite nuclear size of the nuclei is taken into account via a nuclear form factor  $F(q)$ , which represents Fourier transform of the

screened charge distribution of a spherically charged nucleus, see Eq. (22) of Ref. [12] or Eq. (31) of Ref. [4]. The nuclear form factor  $F(q)$  is evaluated with nuclear radii  $R_N$  taken directly from underlying compositions, avoiding the relation  $R_N = aA^{1/3}$  which is inaccurate for the inner crust compositions if  $a = \text{const.}$  is assumed.

The final expression for the relaxation time reads

$$\tau^{-1}(\varepsilon) = \frac{\pi Z^2 e^4 n_i}{\varepsilon p^3} \sqrt{\frac{M}{2\pi T}} \int_{-\infty}^{\varepsilon-m} d\omega e^{-\omega/2T} \frac{f^0(\varepsilon - \omega)}{f^0(\varepsilon)} \times \int_{q_-}^{q_+} dq (q^2 - \omega^2 + 2\varepsilon\omega) \frac{(2\varepsilon - \omega)^2 - q^2}{|q^2 + \Pi_L|^2} \times e^{-\omega^2 M/2q^2 T} e^{-q^2/8MT} S(q) F^2(q), \quad (13)$$

where  $q_{\pm} = |\sqrt{p^2 - (2\omega\varepsilon - \omega^2)} \pm p|$ , and  $\Pi_L \simeq 4e^2 p_F^2/\pi$  is the longitudinal component of the polarization tensor. Note that we neglected the transverse part of the scattering in Eq. (13) as that part is negligibly small in the regime of interest of this work.

If the magnetic field is directed along the  $z$  axis, then the conductivity tensor has the form

$$\hat{\sigma} = \begin{pmatrix} \sigma_0 & -\sigma_1 & 0 \\ \sigma_1 & \sigma_0 & 0 \\ 0 & 0 & \sigma \end{pmatrix}, \quad (14)$$

where the scalar conductivity is given by

$$\sigma = \sigma_0 + \sigma_2 = \frac{e^2}{3\pi^2 T} \int_m^\infty d\varepsilon \frac{p^3}{\varepsilon} \tau f^0(1 - f^0). \quad (15)$$

In the absence of a magnetic field, the conduction becomes isotropic with  $\mathbf{j} = \sigma \mathbf{E}$ , where  $\sigma$  is referred below as scalar conductivity.

At relatively low temperatures  $T \leq 5$  MeV the electronic gas in the inner crust is practically in the degenerate state, therefore we can use the low-temperature limit of Eqs. (12) and (15) by substituting  $\partial f^0/\partial \varepsilon = -f^0(1 - f^0)/T \rightarrow -\delta(\varepsilon - \varepsilon_F)$ , which leads us to the well-known Drude formulas

$$\sigma = \frac{n_e e^2 \tau}{\varepsilon} \Big|_{\varepsilon=\varepsilon_F}, \quad \sigma_0 = \frac{\sigma}{1 + (\omega_c\tau)^2} \Big|_{\varepsilon=\varepsilon_F}, \quad \sigma_1 = (\omega_c\tau) \Big|_{\varepsilon=\varepsilon_F} \sigma_0, \quad (16)$$

where the quantities  $\tau$  and  $\omega_c$  in these equations are evaluated at the Fermi energy  $\varepsilon_F$ .

#### IV. NUMERICAL RESULTS

Numerically, the electrical conductivity is evaluated using the relaxation time Eq. (13). With this relaxation time, we evaluate the components of the conductivity tensor using Eq. (12). Two different regimes of weak and strong magnetic fields arise, which are distinguished by the scalar vs. tensor nature of the conductivity, see Eq. (16). These regimes are distinguished by the value of the Hall parameter  $\omega_c\tau$ . Note that as, by definition,  $\tau$  and  $\omega$  are energy-dependent

quantities, they should be evaluated at the Fermi energy in the degenerate regime, which is the case for  $T \leq 5$  MeV. At high temperatures  $T \geq T_F/3$  where electrons are no longer degenerate, the quantities  $\tau$  and  $\omega$  are evaluated at the thermal energy  $\bar{\varepsilon} = 3T$ , see below (this does not apply, naturally, to the cases where  $\tau$  and  $\omega$  are integrated over the energies where the energy dependence should be kept). In the isotropic case  $\omega_c\tau \ll 1$  one has  $\sigma_1 \ll \sigma_0 \simeq \sigma$ , therefore, all three diagonal components of the conductivity tensor are identical, and the nondiagonal components vanish. In the anisotropic case  $\omega_c\tau \simeq 1$  they are distinct and should be studied separately. Below, we will study the dependence of the conductivity on the density, temperature, and strength of the magnetic field for the selected compositions.

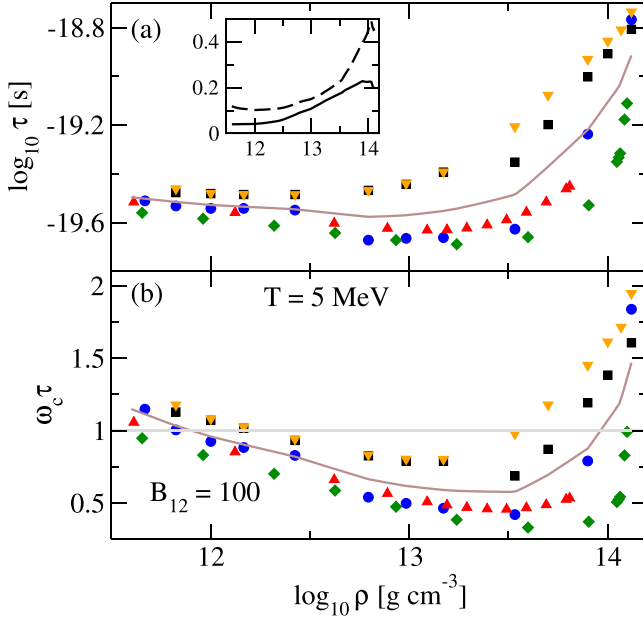


FIG. 5. The relaxation time  $\tau$  and the Hall parameter  $\omega_c \tau$  at the Fermi energy as functions of the mass density for five compositions as labeled in Fig. 1. The temperature is fixed at  $T = 5$  MeV, and the magnetic field is fixed at  $B_{12} = 100$  in (b). The solid lines show the values of these quantities averaged over the five compositions. The solid and dashed curves in the inset show the standard deviations of  $\log_{10} \tau$  and  $\omega_c \tau$ , respectively.

### A. Relaxation time and the Hall parameter

Figure 5 shows the relaxation time  $\tau$  and the Hall parameter  $\omega_c \tau$  for five compositions as functions of the mass density for the temperature  $T = 5$  MeV. Because it corresponds to the degenerate regime for electrons,  $\tau$  and  $\omega_c$  are evaluated at the Fermi energy. To assess the variations in the relaxation time and Hall parameter  $\omega_c \tau$  with the composition we use the same approximations as in Ref. [4], to reduce Eq. (13) to the following form first obtained by Ref. [22]:

$$\tau^{-1} = \frac{4Ze^4 \varepsilon_F}{3\pi} \int_0^{2p_F} \frac{dq}{q} \left(1 - \frac{q^2}{4\varepsilon_F^2}\right) S(q) F^2(q), \quad (17)$$

which implies the scaling

$$\tau \sim Z^{-4/3} n_i^{-1/3}, \quad (18)$$

if we neglect the effects of  $S(q)$  and  $F(q)$ , where we used  $\varepsilon_F = p_F \sim (Zn_i)^{1/3}$ . Because the value of  $Z$  for most of the compositions is fixed at (semi)magic number 40 or 50, Eq. (18) suggests decreasing relaxation times with the density as follows from Fig. 2. However, such behavior is realized only in the low-density domain  $\log_{10} \rho$  [g cm<sup>-3</sup>]  $\leq 12.5 \div 13$ . At higher densities  $\log_{10} \rho$  [g cm<sup>-3</sup>]  $> 13$  the relaxation time reverses from slowly decreasing function to an increasing function of density, which is a consequence of the increasing importance of finite size of the nuclei encoded in the nuclear form factor. It suppresses the electron-ion scattering rates significantly at high densities where the nuclear radii become close to the radii of the Wigner-Seitz cell. This results in larger relaxation times at higher densities.

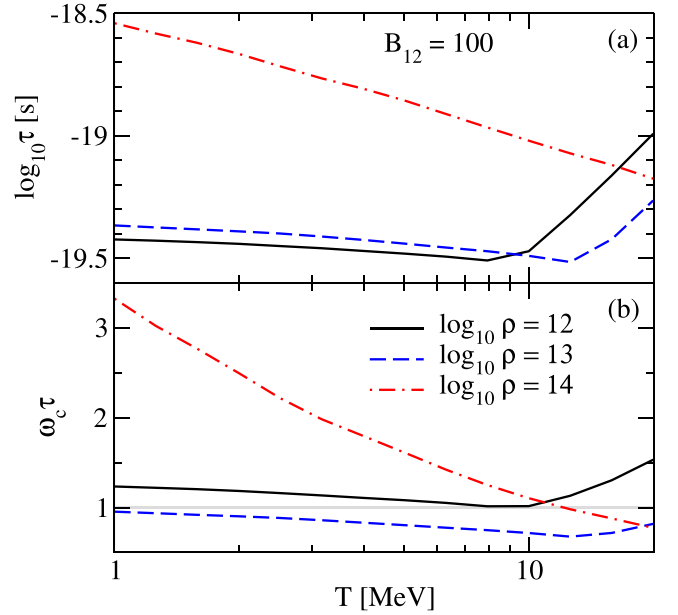


FIG. 6. The relaxation time  $\tau$  and the Hall parameter  $\omega_c \tau$  as functions of the temperature for various values of the mass density for composition DIM\* ( $\tau$  and  $\omega_c$  are evaluated at  $\varepsilon = \varepsilon_F$  if  $T \leq T_F/3$  and at  $\varepsilon = 3T$  if  $T \geq T_F/3$ , see the discussion in the text). In (b) the magnetic field is fixed at  $B_{12} = 100$ .

This effect is stronger for two models DIM and DIM\* as these models predict a significant increase in the mass number and size of nuclei with the density in the high-density regime, as seen from Fig. 1. Figure 8(a) shows the relaxation time for two models DIM\* and Bsk24, which predict the same values of  $Z$  and very close values of  $n_i$ , therefore, the differences in the relaxation times predicted by these models can be attributed to the difference in the values of  $A$ , which manifests itself through the nuclear form factor. Indeed, as seen from the figure, the relaxation times for both models are very similar and do follow the scaling  $\tau \sim n_i^{-1/3}$  in the case where the factor  $F(q)$  is set to one (empty symbols) whereas in the full calculation (filled symbols)  $\tau$  increases with the density with different slopes for different models, thus the scaling (18) fails. The scaling (18) works qualitatively well for outer crust matter, where the effect of the form factor is small for nuclei with small  $A$  [4].

The solid line in Fig. 5(a) shows the average logarithmic relaxation time scale computed as  $\langle \log_{10} \tau \rangle = \sum_{i=1}^5 \log_{10} \tau_i / 5$ , where  $\tau_i$  are the relaxation times for the five compositions interpolated in the density range  $11.6 \leq \log_{10} \rho$  [g cm<sup>-3</sup>]  $\leq 14.12$ . Similarly, the solid line in Fig. 5(b) shows the average value of  $\omega_c \tau$ . In addition, we show the standard deviations of these quantities from their average values in the inset located in Fig. 5(a). The solid line shows the standard deviation for  $\log_{10} \tau$ , and the dashed line—that for  $\omega_c \tau$ . We compute the standard deviation  $s_a$  of a quantity  $a$  using the formula  $s_a = \sqrt{\sum_{i=1}^5 (a_i - \langle a \rangle)^2 / 5}$ , where  $\langle a \rangle$  is the average value over the five compositions.

Figure 6 shows the temperature dependence of the relaxation time and the Hall parameter for several densities for the

composition DIM\*. Here we extrapolate our results of low-temperature matter to higher temperatures (up to 20 MeV) making a crude assumption that the composition of matter does not change significantly with the temperature at the given density. As the matter is partially degenerate at temperatures  $T \geq 10$  MeV at low densities, we evaluate the quantities  $\tau$  and  $\omega_c$  at the Fermi energy at temperatures  $T \leq T^*$ , and at the thermal energy of ultrarelativistic electrons  $\bar{\varepsilon} = 3T$  at  $T \geq T^*$ , where  $T^* = T_F/3$  is the transition temperature from the nondegenerate to the degenerate regime and corresponds to the requirement that the Fermi energy becomes equal to the thermal energy of a nondegenerate gas, i.e.,  $\varepsilon_F \simeq T_F = 3T$  [4]. It is seen that  $\tau$  decreases with the temperature in the strongly degenerate regime  $T \leq T^*$  and increases in the semidegenerate regime  $T \geq T^*$ , which leads to a minimum at  $T \sim T^*$  in the conductivity. The first effect originates from the structure factor  $S(q)$  and, at very high densities also from the nuclear form factor  $F(q)$ . In the semidegenerate regime, the temperature dependence of  $\tau$  is dominated by the energy increase of electrons with temperature, and  $\tau$  becomes increasing with temperature.

From the bottom panels of Figs. 5 and 6 we see that for magnetic field  $B_{12} \equiv B/(10^{12}\text{G}) = 100$  the factor  $\omega_c \tau$  is of the order of unity in the whole inner crust. This implies that the effect of anisotropy should become important at such values of fields. We see that the effects of anisotropy in the inner crust are less pronounced than in the low-density outer crust, where the anisotropy becomes important already for  $B_{12} \geq 0.01$  [4].

### B. Conductivity in the low-field limit

We start with the results on the density dependence of the scalar conductivity at a fixed temperature. Figure 7 shows the scalar conductivity as a function of the density for  $T = 5$  MeV. Despite the nonmonotonic behavior of the relaxation time with the density, the increase of density of the states close to the Fermi surface leads to an increase of conductivity with matter density, as seen from the first formula of Eq. (16). Similar to the case of the relaxation time, comparisons can be made among the various compositions and the effects of various factors on the conductivity. Given that for most of the compositions  $Z$  is fixed at a (semi)magic number, and the ion number density  $n_i$  has similar values, the dependence of  $\sigma$  on the density for any given composition is controlled mainly by the dependence of the values of  $A$  on density, which affects the conductivities by means of the nuclear form factors, as mentioned above. Figure 8(b) shows the conductivity for two models DIM\* and Bsk24 and two cases with  $F(q) = 1$  and full  $F(q)$ , which confirm the statements above. We see that for  $F(q) = 1$  the scalar conductivity would increase as a power law with the density following the universal approximate scaling  $\sigma \propto \rho^{1/4}$ , whereas for full  $F(q)$  a much faster increase of the conductivity at high densities is observed. The slopes are composition dependent.

In addition, we show in Fig. 7 the (logarithmic) conductivity averaged over the five compositions and the standard deviation for  $\log_{10} \sigma$  in the inset. As expected, the standard deviation rises with density as the differences between the

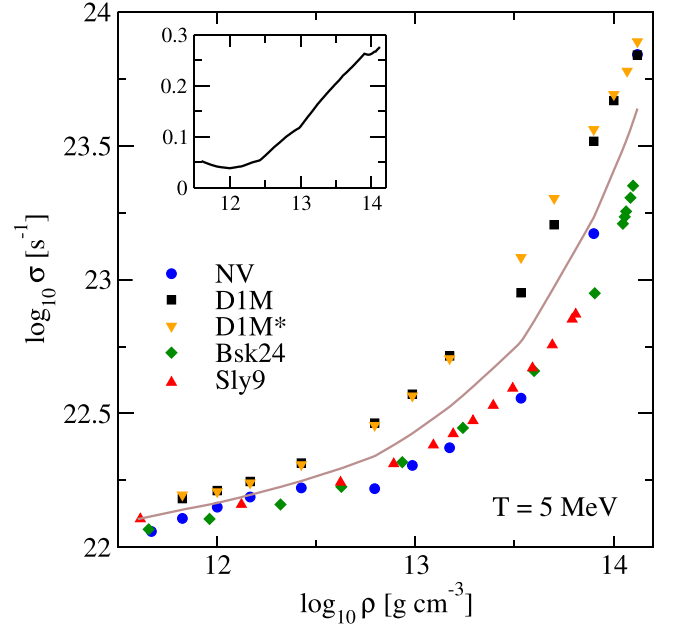


FIG. 7. Dependence of the scalar conductivity on density for five compositions. The temperature is fixed at  $T = 5$  MeV. The solid line shows the logarithm of the conductivity averaged over the five compositions, and the inset shows the standard deviation for  $\log_{10} \sigma$ .

compositions with regard to predicted values of  $Z$ ,  $A$ , and  $n_i$  increase with density. The deviations rise sharply beyond  $\log_{10} \rho [\text{g cm}^{-3}] \geq 13$ , but the overall deviation remains below 25%, except close to the crust-core interface, where nonspherical nuclei are expected.

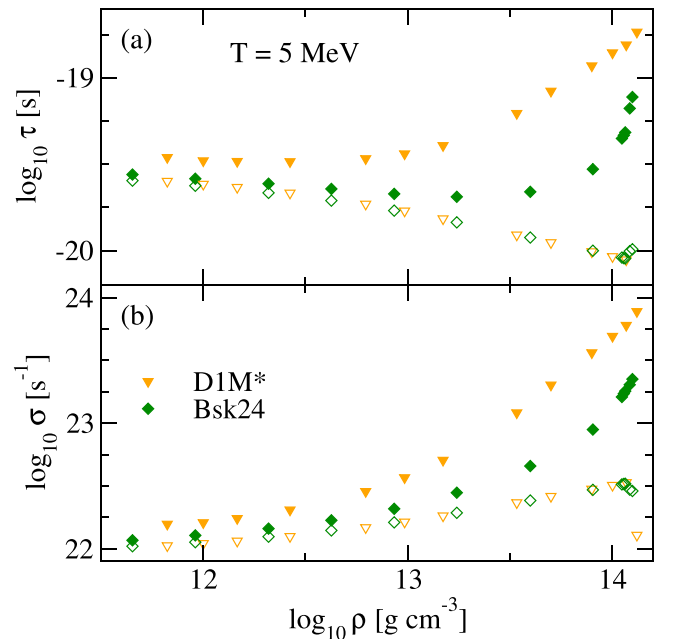


FIG. 8. (a) Dependence of the relaxation time and (b) the scalar conductivity on density for two models evaluated with full nuclear form factor  $F(q)$  (filled symbols) and with  $F(q) = 1$  (empty symbols). The temperature is fixed at  $T = 5$  MeV.

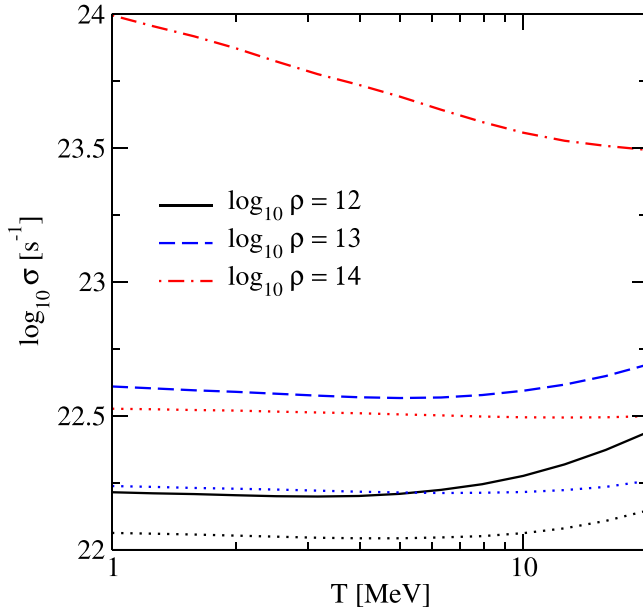


FIG. 9. The temperature dependence of the scalar conductivity for various values of the density for composition D1M\*. The dotted lines show the corresponding values of  $\sigma$  in the case where the effect of the nuclear form factor is neglected.

The temperature dependence of the conductivity at fixed values of the density is shown in Fig. 9. This figure allows for extrapolation to larger temperatures where the compositions of the matter used are not realistic as they have been derived at zero temperature and assuming matter without neutrinos. In the range of temperatures where the compositions are realistic  $0 \leq T \leq 5$  MeV (and beyond up to 10 MeV) the temperature dependence of the conductivity is very weak, except at very high densities and models with very large values of  $A$ , where the nuclear form factor plays the key role in the scattering rates as discussed in the previous subsection. To illustrate this, we show in Fig. 9 the corresponding values of  $\sigma$  in the case where the effect of nuclear form factor is neglected, i.e.,  $F(q) = 1$ . We clearly see that the form factor affects not only the magnitude of the conductivity at high densities, but also modifies its temperature dependence by making it much steeper than at low density. Numerically we find that for the model D1M\* the form factor increases the conductivity by factors of 1.4, 2.3, and between 15 and 30 at densities  $\rho = 10^{12}$ ,  $\rho = 10^{13}$ , and  $\rho = 10^{14}$  g cm $^{-3}$ , respectively, and for  $5 \geq T \geq 1$  MeV. These factors are similar for the model D1M, which predicts very large values of  $A$  at  $\rho \geq 10^{13}$  g cm $^{-3}$  as well. The remaining models are characterized by smaller values of  $A$ , therefore the modifications due to the nuclear form factor are less pronounced for  $\rho \simeq 10^{14}$  g cm $^{-3}$ .

### C. Conductivities in the high-field limit

We now consider the density dependence of the conductivity in the anisotropic case where the magnetic fields are large. Figure 10 shows the density dependence of the  $\sigma_0$  component for two values of the magnetic field ( $B_{12} = 10, 100$ ) for

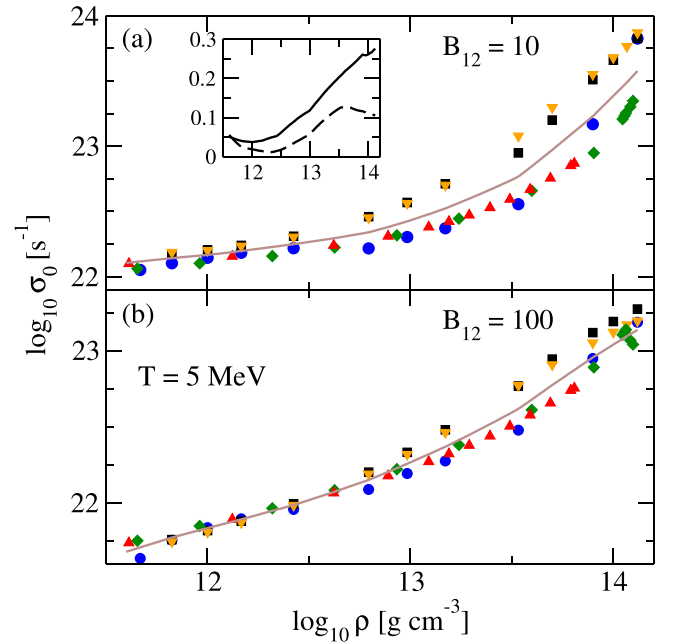


FIG. 10. Dependence of  $\sigma_0$  component of the electrical conductivity tensor on density for five compositions. The labeling of the curves is as in Fig. 7. The values of the temperature and the magnetic field are indicated in the plot. The solid lines in each panel show the averages of  $\log_{10} \sigma_0$  over the five compositions. The solid and dashed curves in the inset show the standard deviation of  $\log_{10} \sigma_0$  for  $B_{12} = 10$  and  $B_{12} = 100$ , respectively.

compositions considered. The temperature is fixed at  $T = 5$  MeV. The same for the component  $\sigma_1$  is shown in Fig. 11.

For the magnetic field  $B_{12} = 10$  we have  $\omega_c \tau \ll 1$ , which implies essentially isotropic conduction. In this case, the component  $\sigma_0$  is almost identical to the scalar conductivity  $\sigma$  as seen from Figs. 7 and 10, and the values of  $\sigma_1$  are much lower. For  $B_{12} \gtrsim 30$  the anisotropy already sets in, as can be seen from Fig. 12, and for the value  $B_{12} = 100$  the transverse components of the conductivity  $\sigma_0$  and  $\sigma_1$  have the same order of magnitude, as already  $\omega_c \tau \sim 1$ . The averages of  $\log_{10} \sigma_0$  and  $\log_{10} \sigma_1$  and their standard deviations are also shown in Figs. 10 and 11.

We show the magnetic field dependence of the components of conductivities for fixed values of temperature and density in Fig. 12. According to Eq. (16)  $\sigma_1$  is proportional to the magnetic field in the isotropic regime whereas  $\sigma_0$  is independent of it; these features are seen in Fig. 12. In general, we see that the effect of the magnetic field on the conduction in the inner crust up to the limit of nonquantizing fields  $B_{12} \simeq 100$  is not as significant as it was the case for the outer crust, which becomes totally anisotropic for  $B_{12} \geq 10$  [4].

The temperature dependence of the conductivity components  $\sigma_0$  and  $\sigma_1$  is shown in Fig. 13 for fixed magnetic field  $B_{12} = 100$ . These components depend weakly on the temperature, because the temperature dependence of the scalar conductivity  $\sigma$  and that of the product  $\omega_c \tau$  partially cancel each other.



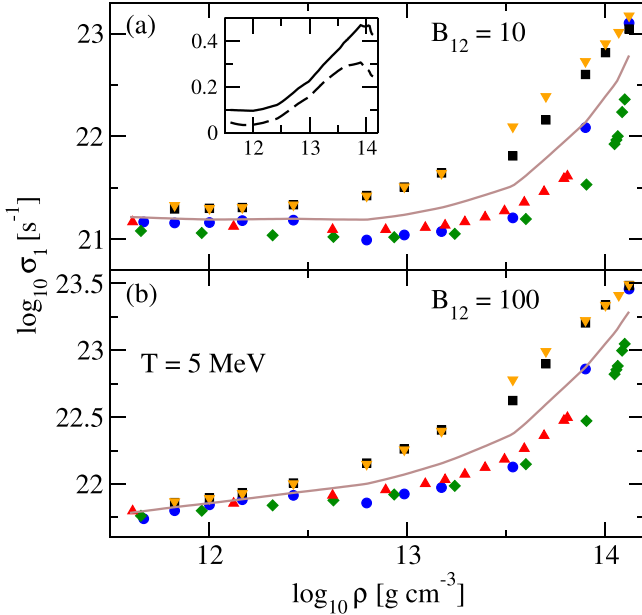


FIG. 11. Dependence of  $\sigma_1$  component of the electrical conductivity tensor on density for four compositions. The labeling of the curves is as in Fig. 7. The values of the temperature and the magnetic field are indicated in the plot. The solid lines in each panel show the averages of  $\log_{10} \sigma_1$  over the five compositions. The solid and dashed curves in the inset show the standard deviation of  $\log_{10} \sigma_1$  for  $B_{12} = 10$  and  $B_{12} = 100$ , respectively.

#### D. Remarks on electron-neutron scattering

In addition to the Coulomb scattering of electrons off the nuclei studied in detail above, electrons will be scattered by neutrons due to their anomalous magnetic moment  $g_n = -1.91$ . The ratio of the respective relaxation times can be estimated from the transition probabilities  $W_{ep}$  and  $W_{en}$  for electron-proton and electron-neutron scattering, which were computed in Ref. [23] and are given by their Eqs. (48) and (49). The ratio of the corresponding relaxation times, up to a factor  $O(1)$ , is given by

$$\frac{\tau_{en}}{\tau_{ep}} \sim \frac{W_{ep}Z}{W_{en}N} \simeq \frac{1}{2g_n^2} \left( \frac{m_N}{p_F} \right)^2 \frac{Z}{N}, \quad (19)$$

where  $m_N$  is the neutron mass and  $N$  is the number of neutrons in a Wigner-Seitz cell. For an estimate, we use the model DIM and Table II of Ref. [7] in the range  $0.006 \geq n_B \geq 0.06$  [ $\text{fm}^{-3}$ ] (which corresponds to the mass density range  $12 \leq \log_{10} \rho$  [ $\text{g cm}^{-3}$ ]  $\leq 14$ ). We then find that  $0.185 \geq Z/N \geq 0.04$  and  $1175 \geq (m_N/p_F)^2 \geq 138$ , assuming bare neutron mass  $m_N = 939$  MeV, and

$$30 \geq \frac{\tau_{en}}{\tau_{ep}} \geq 0.8. \quad (20)$$

From this elementary estimate, we conclude that the electron-neutron interaction can appreciably contribute to the conductivity close to the crust-core transition, but is subdominant at lower densities.

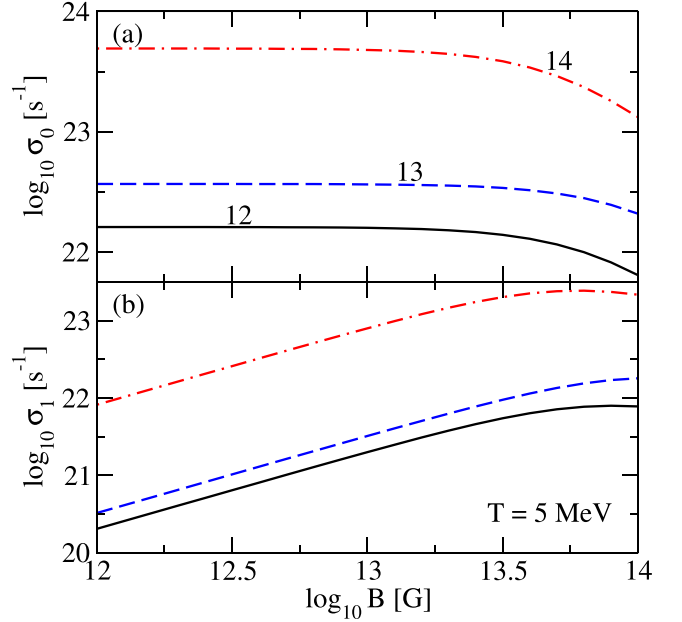


FIG. 12. The dependence of  $\sigma_0$  and  $\sigma_1$  components of the electrical conductivity tensor on the magnetic field at fixed temperature and for various values of the density indicated on the plot by their logarithm for composition DIM\*.

#### V. CONCLUSIONS

In this work, we extended the study of the finite-temperature conductivity of the outer crust of compact stars in the liquid regime in magnetic fields [4] to the inner crust characterized by a neutron drip component that forms a separate fluid. Because of higher densities, the electrons in the

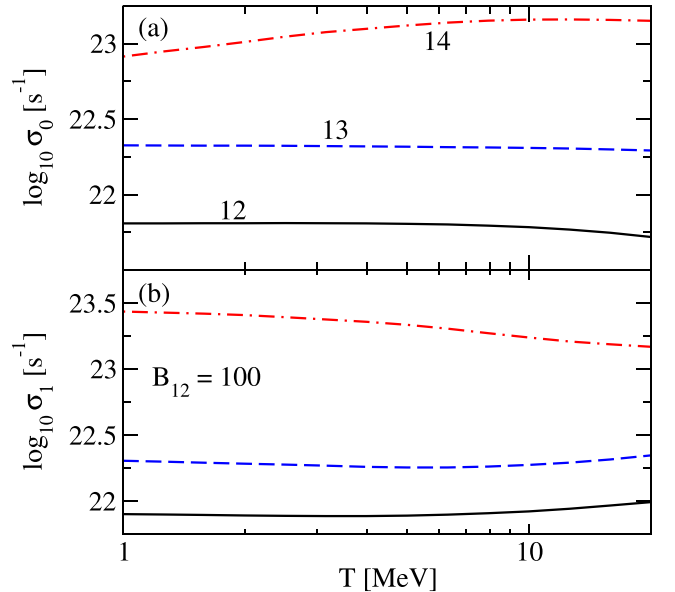


FIG. 13. The dependence of  $\sigma_0$  and  $\sigma_1$  components of the electrical conductivity tensor on the temperature at fixed magnetic field for various values of the density indicated on the plot by their logarithm for composition DIM\*.

inner crust are mostly in the degenerate regime within the range of temperatures in which the composition of the inner crust computed at zero temperature can still be applied ( $T \leq T_{\text{tr}} \simeq 5$  MeV). Nevertheless, our extrapolation beyond this range shows that there is a minimum in the conductivity at the transition from the degenerate to the nondegenerate regime, which was also the case in the outer crust. Of course, a self-consistent computation of the conductivity of multicomponent nuclear plasma in this regime is required to draw definitive conclusions.

To assess the uncertainties in the conductivities due to the composition we have taken an average over the five adopted compositions (NV, Bsk24, D1M, D1M\*, and Sly9) and computed the standard deviation. The deviations are below 10% for densities  $\log_{10} \rho [\text{g cm}^{-3}] \leq 12.5$  and increase up to 25% for higher densities. Exceptions are very high densities  $\log_{10} \rho [\text{g cm}^{-3}] \geq 14$  where standard deviations can increase up to 40%, but one anticipates nonspherical nuclei at such densities. Our analysis shows that this scatter among different compositions affects the transport quantities through the nuclear form factor (i.e., finite nuclear size). It is the dominant agent that determines the behavior of the conductivity at high densities.

The anisotropy of transport becomes sizable for magnetic fields  $B_{12} \geq 30$  and low densities as well as for larger fields  $B_{12} \geq 50$  at higher densities. The field diminishes the  $\sigma_0$  component of the conductivity and the nondiagonal component  $\sigma_1$  becomes of the order of  $\sigma_0$  at  $B_{12} \simeq 100$ .

Dissipation through conductivity may or may not be important depending on the effectiveness of the other channels of dissipation appearing in the relativistic fluid dynamics description of BNS mergers, supernovas, and protoneutron stars. Recent microscopic work shows that the bulk viscosity is a potentially important channel of dissipation [24–26] as can be seen from the estimates of relevant damping time scales [27,28] and implementations in the relativistic hydrodynamics simulations [29,30].

Looking ahead, it would be interesting to apply the formalism used in this work to study the conductivity of the star's core. At low temperatures, the core is superconducting, and conductivity and screening are affected by heterogeneities on the scales of the order of  $10^2$ – $10^4$  fm, which are introduced by

the flux tubes [31] in the case of type-II and normal domains in the case of type-I superconductivity [32].

To conclude, we have quantified the conductivity of the warm inner crust of a compact star within the Boltzmann quasiparticle transport of electrons in the liquid phase of inner crust matter taking into account the screening of electron-ion interaction, finite nuclear size, ion structure factor, and magnetic fields. Five different compositions were studied to assess the dependence of the results on adopted composition. In the future, this study can be extended to higher temperatures by adopting compositions that have been derived at finite temperature and account for the multi-ion composition of matter, which includes  $\alpha$  particles and other light clusters.

## ACKNOWLEDGMENTS

The authors gratefully acknowledge the collaborative research Grant No. 96 839 of Volkswagen Foundation (Hannover, Germany). We thank Jonas Dittrich for testing the code used in this work and N. Chamel, C. Mondal, and A. Raduta for useful communications. A.S. acknowledges support through Deutsche Forschungsgemeinschaft Grant No. SE 1836/5-2, the Polish NCN Grant No. 2020/37/B/ST9/01937, and thanks the Institute for Nuclear Theory at the University of Washington for its kind hospitality, stimulating research environment, and partial support by the INT's U.S. Department of Energy Grant No. DE-FG02-00ER41132.

## APPENDIX: TABLES OF TRANSPORT PARAMETERS

In this Appendix we provide numerical results for the density dependence of the components of conductivity tensor along with relaxation time and anisotropy parameter for the five models studied in this work. Tables are given for fixed temperatures  $T = 1$  and  $T = 5$  MeV, which bracket the range to which the current study is applicable and fixed value of magnetic field  $B_{12} = 100$ . Table I is computed with model NV, Table II with model D1M, Table III with model D1M\*, Table IV with model Bsk24 and Table V with model Sly9.

TABLE I. Model NV and  $B_{12} = 100$ .

$\log_{10} \rho$	$T = 1$ MeV					$T = 5$ MeV				
	$\log_{10} \tau$	$\omega_c \tau$	$\log_{10} \sigma$	$\log_{10} \sigma_0$	$\log_{10} \sigma_1$	$\log_{10} \tau$	$\omega_c \tau$	$\log_{10} \sigma$	$\log_{10} \sigma_0$	$\log_{10} \sigma_1$
11.825	−19.482	1.128	22.115	21.757	21.810	−19.532	1.005	22.108	21.754	21.800
12.001	−19.491	1.039	22.158	21.839	21.857	−19.542	0.925	22.150	21.836	21.844
12.167	−19.491	0.994	22.198	21.898	21.897	−19.542	0.883	22.188	21.894	21.882
12.425	−19.497	0.934	22.234	21.961	21.932	−19.549	0.829	22.222	21.956	21.915
12.795	−19.632	0.592	22.224	22.093	21.867	−19.672	0.540	22.219	22.087	21.858
12.985	−19.624	0.547	22.316	22.202	21.941	−19.665	0.498	22.306	22.192	21.925
13.173	−19.620	0.512	22.387	22.285	21.996	−19.662	0.464	22.372	22.274	21.973
13.533	−19.579	0.469	22.584	22.497	22.169	−19.627	0.420	22.557	22.477	22.127
13.900	−19.105	1.070	23.290	22.959	22.988	−19.237	0.790	23.172	22.948	22.860
14.120	−18.364	4.654	24.236	22.880	23.548	−18.767	1.838	23.841	23.186	23.458

TABLE II. Model DIM and  $B_{12} = 100$ .

$\log_{10} \rho$	$T = 1 \text{ MeV}$					$T = 5 \text{ MeV}$				
	$\log_{10} \tau$	$\omega_c \tau$	$\log_{10} \sigma$	$\log_{10} \sigma_0$	$\log_{10} \sigma_1$	$\log_{10} \tau$	$\omega_c \tau$	$\log_{10} \sigma$	$\log_{10} \sigma_0$	$\log_{10} \sigma_1$
11.825	-19.421	1.285	22.186	21.759	21.870	-19.477	1.128	22.182	21.757	21.861
12.001	-19.424	1.223	22.219	21.819	21.908	-19.481	1.071	22.212	21.817	21.897
12.167	-19.427	1.162	22.255	21.882	21.949	-19.485	1.016	22.246	21.879	21.935
12.425	-19.425	1.072	22.331	21.997	22.029	-19.485	0.932	22.315	21.993	22.007
12.795	-19.400	0.965	22.495	22.208	22.194	-19.468	0.826	22.464	22.201	22.156
12.985	-19.369	0.937	22.616	22.341	22.313	-19.443	0.790	22.572	22.331	22.262
13.173	-19.307	0.963	22.775	22.489	22.474	-19.393	0.790	22.715	22.479	22.404
13.533	-	-	-	-	-	-19.352	0.687	22.951	22.767	22.624
13.700	-	-	-	-	-	-19.198	0.871	23.205	22.944	22.899
13.900	-	-	-	-	-	-19.002	1.192	23.517	23.118	23.205
14.001	-	-	-	-	-	-18.907	1.383	23.669	23.191	23.340
14.120	-	-	-	-	-	-18.807	1.606	23.839	23.273	23.485

TABLE III. Model DIM\* and  $B_{12} = 100$ .

$\log_{10} \rho$	$T = 1 \text{ MeV}$					$T = 5 \text{ MeV}$				
	$\log_{10} \tau$	$\omega_c \tau$	$\log_{10} \sigma$	$\log_{10} \sigma_0$	$\log_{10} \sigma_1$	$\log_{10} \tau$	$\omega_c \tau$	$\log_{10} \sigma$	$\log_{10} \sigma_0$	$\log_{10} \sigma_1$
11.825	-19.402	1.349	22.199	21.745	21.878	-19.461	1.178	22.196	21.744	21.868
12.001	-19.423	1.234	22.214	21.810	21.903	-19.480	1.081	22.208	21.807	21.892
12.167	-19.426	1.172	22.250	21.872	21.943	-19.484	1.025	22.241	21.870	21.929
12.425	-19.424	1.081	22.325	21.986	22.022	-19.485	0.941	22.309	21.983	22.002
12.795	-19.401	0.972	22.487	22.196	22.185	-19.468	0.833	22.456	22.189	22.148
12.985	-19.366	0.953	22.609	22.327	22.307	-19.440	0.804	22.566	22.318	22.256
13.173	-19.307	0.977	22.764	22.472	22.463	-19.392	0.802	22.705	22.462	22.395
13.533	-19.069	1.340	23.203	22.755	22.883	-19.206	0.978	23.083	22.771	22.779
13.700	-18.891	1.810	23.476	22.845	23.103	-19.077	1.178	23.304	22.907	22.992
13.900	-18.666	2.668	23.814	22.903	23.330	-18.930	1.451	23.561	23.051	23.223
14.001	-18.541	3.324	23.996	22.915	23.437	-18.855	1.613	23.692	23.121	23.337
14.068	-18.460	3.828	24.119	22.924	23.507	-18.809	1.714	23.779	23.170	23.411
14.120	-	-	-	-	-	-18.735	1.947	23.889	23.195	23.491

TABLE IV. Model Bsk24 and  $B_{12} = 100$ .

$\log_{10} \rho$	$T = 1 \text{ MeV}$					$T = 5 \text{ MeV}$				
	$\log_{10} \tau$	$\omega_c \tau$	$\log_{10} \sigma$	$\log_{10} \sigma_0$	$\log_{10} \sigma_1$	$\log_{10} \tau$	$\omega_c \tau$	$\log_{10} \sigma$	$\log_{10} \sigma_0$	$\log_{10} \sigma_1$
11.655	-19.514	1.054	22.078	21.752	21.776	-19.560	0.947	22.067	21.750	21.762
11.962	-19.538	0.923	22.119	21.850	21.817	-19.584	0.831	22.106	21.847	21.800
12.320	-19.568	0.779	22.176	21.969	21.862	-19.613	0.702	22.160	21.963	21.840
12.627	-19.598	0.649	22.245	22.092	21.905	-19.643	0.586	22.226	22.082	21.877
12.934	-19.628	0.525	22.340	22.234	21.955	-19.672	0.474	22.318	22.220	21.921
13.240	-19.644	0.426	22.472	22.399	22.030	-19.689	0.384	22.446	22.380	21.986
13.599	-19.610	0.371	22.695	22.639	22.209	-19.660	0.331	22.659	22.610	22.148
13.905	-19.459	0.436	23.008	22.933	22.572	-19.529	0.371	22.949	22.890	22.472
14.047	-19.244	0.650	23.307	23.154	22.966	-19.351	0.507	23.209	23.104	22.821
14.056	-19.220	0.680	23.337	23.172	23.004	-19.333	0.525	23.235	23.123	22.855
14.063	-19.199	0.711	23.362	23.185	23.037	-19.316	0.543	23.255	23.137	22.883
14.085	-19.024	1.181	23.448	23.069	23.141	-19.177	0.829	23.306	23.067	22.998
14.098	-18.934	1.490	23.517	23.008	23.182	-19.111	0.991	23.351	23.040	23.048

TABLE V. Model Sly9 and  $B_{12} = 100$ .

$\log_{10} \rho$	$T = 1 \text{ MeV}$					$T = 5 \text{ MeV}$				
	$\log_{10} \tau$	$\omega_c \tau$	$\log_{10} \sigma$	$\log_{10} \sigma_0$	$\log_{10} \sigma_1$	$\log_{10} \tau$	$\omega_c \tau$	$\log_{10} \sigma$	$\log_{10} \sigma_0$	$\log_{10} \sigma_1$
11.613	-19.464	1.190	22.121	21.736	21.813	-19.516	1.057	22.106	21.736	21.798
12.123	-19.510	0.954	22.176	21.894	21.875	-19.559	0.852	22.160	21.891	21.855
12.623	-19.555	0.738	22.263	22.073	21.942	-19.603	0.661	22.243	22.064	21.915
12.891	-19.576	0.632	22.334	22.188	21.990	-19.624	0.566	22.312	22.176	21.956
13.091	-19.582	0.569	22.408	22.285	22.041	-19.631	0.508	22.382	22.270	22.002
13.191	-19.580	0.545	22.452	22.339	22.076	-19.630	0.486	22.424	22.321	22.032
13.291	-19.571	0.529	22.504	22.397	22.121	-19.623	0.469	22.473	22.377	22.072
13.393	-19.555	0.520	22.565	22.461	22.178	-19.610	0.459	22.530	22.438	22.123
13.491	-19.530	0.524	22.634	22.529	22.248	-19.589	0.457	22.594	22.503	22.185
13.591	-19.493	0.542	22.717	22.605	22.340	-19.558	0.467	22.670	22.576	22.265
13.691	-19.442	0.578	22.813	22.688	22.450	-19.516	0.488	22.756	22.655	22.362
13.791	-19.377	0.639	22.922	22.774	22.579	-19.462	0.525	22.852	22.738	22.475
13.809	-19.364	0.653	22.943	22.789	22.604	-19.451	0.534	22.871	22.753	22.497

- [1] B. P. Abbott, R. Abbott, T. D. Abbot *et al.* ( LIGO Scientific, Virgo), *Phys. Rev. X* **9**, 011001 (2019).
- [2] A. Schmitt and P. Shternin, in *Astrophysics and Space Science Library*, edited by L. Rezzolla, P. Pizzochero, D. I. Jones, N. Rea, and I. Vidaña (Springer, New York, 2018), Vol. 457, p. 455.
- [3] A. Y. Potekhin, J. A. Pons, and D. Page, in *The Strongest Magnetic Fields in the Universe*, Space Sciences Series of ISSI, edited by V. S. Beskin, A. Balogh, M. Falanga, M. Lyutikov, S. Mereghetti, T. Piran, and R. A. Treumann (Springer, New York, 2018), Vol. 54, pp. 245–297.
- [4] A. Harutyunyan and A. Sedrakian, *Phys. Rev. C* **94**, 025805 (2016).
- [5] A. Harutyunyan, A. Nathanail, L. Rezzolla, and A. Sedrakian, *Eur. Phys. J. A* **54**, 191 (2018).
- [6] J. W. Negele and D. Vautherin, *Nucl. Phys. A* **207**, 298 (1973).
- [7] C. Mondal, X. Viñas, M. Centelles, and J. N. De, *Phys. Rev. C* **102**, 015802 (2020).
- [8] J. M. Pearson, N. Chamel, A. Y. Potekhin, A. F. Fantina, C. Ducoin, A. K. Dutta, and S. Goriely, *MNRAS* **481**, 2994 (2018).
- [9] A. R. Raduta and F. Gulminelli, *Nucl. Phys. A* **983**, 252 (2019).
- [10] N. Chamel, A. F. Fantina, J. M. Pearson, and S. Goriely, *Phys. Rev. C* **84**, 062802(R) (2011).
- [11] M. R. Pelicer, M. Antonelli, D. P. Menezes, and F. Gulminelli, *MNRAS* **521**, 743 (2023).
- [12] N. Itoh, Y. Kohyama, N. Matsumoto, and M. Seki, *Astrophys. J.* **285**, 758 (1984).
- [13] A. Y. Potekhin, *Astron. Astrophys.* **351**, 787 (1999).
- [14] G. Baym, H. A. Bethe, and C. J. Pethick, *Nucl. Phys. A* **175**, 225 (1971).
- [15] S. Typel, G. Röpke, T. Klähn, D. Blaschke, and H. H. Wolter, *Phys. Rev. C* **81**, 015803 (2010).
- [16] M. Hempel, J. Schaffner-Bielich, S. Typel, and G. Röpke, *Phys. Rev. C* **84**, 055804 (2011).
- [17] M. Hempel, T. Fischer, J. Schaffner-Bielich, and M. Liebendörfer, *Astrophys. J.* **748**, 70 (2012).
- [18] X.-H. Wu, S.-B. Wang, A. Sedrakian, and G. Röpke, *J. Low Temp. Phys.* **189**, 133 (2017).
- [19] T. Fischer, S. Typel, G. Röpke, N.-U. F. Bastian, and G. Martínez-Pinedo, *Phys. Rev. C* **102**, 055807 (2020).
- [20] A. Sedrakian, *Eur. Phys. J. A* **56**, 258 (2020).
- [21] E. M. Lifshitz and L. P. Pitaevskii, *Physical kinetics* (Butterworth-Heinemann, Oxford, 1981).
- [22] R. Nandkumar and C. J. Pethick, *Mon. Not. R. Astron. Soc.* **209**, 511 (1984).
- [23] E. Flowers and N. Itoh, *Astrophys. J.* **230**, 847 (1979).
- [24] M. G. Alford, L. Bovard, M. Hanauske, L. Rezzolla, and K. Schwenzer, *Phys. Rev. Lett.* **120**, 041101 (2018).
- [25] M. G. Alford and S. P. Harris, *Phys. Rev. C* **100**, 035803 (2019).
- [26] M. Alford, A. Harutyunyan, and A. Sedrakian, *Phys. Rev. D* **100**, 103021 (2019). *Particles* **3**, 500 (2020). *Phys. Rev. D* **108**, 083019 (2023).
- [27] M. G. Alford and A. Haber, *Phys. Rev. C* **103**, 045810 (2021).
- [28] M. Alford, A. Harutyunyan, and A. Sedrakian, *Particles* **5**, 361 (2022).
- [29] E. R. Most, A. Haber, S. P. Harris, Z. Zhang, M. G. Alford, and J. Noronha, *arXiv:2207.00442*.
- [30] T. Celora, I. Hawke, P. C. Hammond, N. Andersson, and G. L. Comer, *Phys. Rev. D* **105**, 103016 (2022).
- [31] D. Kobayakov, *Phys. Rev. C* **108**, L062801 (2023).
- [32] A. Sedrakian, *Phys. Rev. D* **71**, 083003 (2005).